The influence of geosynthetics design on the behavior of reinforced soil embankments subjected to rockfall impacts

Oltion Korini, Marion Bost, Jean-Pierre Rajot, Yassine Bennani, Nicolas Freitag

The influence of geosynthetics design on the behavior of reinforced soil embankments subjected to rockfall impacts

Oltion Korini[1], Marion Bost[1], Jean-Pierre Rajot[1], Yassine B. Braouli[2], Nicolas Freitag[2]

[1]GERS-RRO, Univ Gustave Eiffel, 25 avenue François Miterrand, F-69675 Lyon, France
[2]Terre Armée SAS, 280 avenue Napoleon Bonaparte, Rueil Malmaison 92500, France

Corresponding author: Oltion Korini (oltion.korini@gmail.com)

Abstract. Rockfall hazard in mountainous areas requires the construction of protective structures for the buildings or transport facilities. Reinforced soil embankments can be effective protections against rockfalls due to the combination of the damping characteristics of the soil and the tensile resistance of the reinforcements. Following the advances in soil reinforcements, the research is ongoing for this type of structures aiming to optimize their shape and reinforcement design. In order to study the influence of the different geosynthetics design, two reinforced soil embankments are tested experimentally. The embankments had vertical facings and a slenderness ratio of two with the purpose to reduce the footprint of the conventional trapezoidal shape. Embankment 1 had two vertical layers of geogrids that divided its cross section in three equal parts, while Embankment 2 had multiple geogrid strips installed horizontally close to the front facing. Horizontal impact tests are performed on the two embankments using reinforced concrete blocks as impactors with the aid of a pendulum device. Several instruments and sensors are used to monitor the behavior of the embankments, namely accelerometers, pressure sensors, strain gauges, rapid cameras and a laser scanner. During the tests, the two embankments experienced local shearing at the impact position and overall backward leaning. Moreover, a waves' propagation effect is observed during the first moments of the impact at the sensors installed in the embankments. The speed of the propagation of these waves appears to be influenced by the reinforcement design of the embankments. After the tests, Embankment 2 was less deformed than Embankment 1, which is attributed to their different reinforcement design. According to the strain gauges measurements, the geogrids of Embankment 2 were better mobilized in the vicinity of the impact compared to the ones of Embankment 1. These tests showed that the geogrids installed in horizontal position close to the front facing are more efficient compared to the ones installed vertically and deeper in the embankment.

Keywords: rockfall protection, reinforced soil embankment, geosynthetics, horizontal impact, impact waves

Highlights:

- The tested reinforced soil embankments have vertical facings for foundation optimization
- The reinforced soil embankments have a slenderness ratio of two
- The geosynthetics design plays an important role in the impact response of embankments

- The tested embankments are vulnerable with regard to structural stability
- The impact waves propagation is demonstrated by accelerometers, pressure sensors and strain gauges

1 Introduction

Countless engineering structures (habitations, roads, etc.) have been constructed in areas that are prone to rockfalls. In order to prevent life loss and material damage, protective structures that are able to stop or deviate the falling rock blocks are built at the predicted trajectory of the blocks. These protective systems are called passive. Different passive protection systems are implemented depending on the site conditions and budget (Chen et al., 2013; Lambert and Bourrier, 2013; Lambert and Kister, 2018). Reinforced soil embankments are one of the passive protection systems that may be used to stop falling blocks with kinetic energies that reach up to 30 MJ (Descoudres, 1997). These structures are massive barriers that are usually built adjacent to the slopes for inhibiting the eventual falling rocks to reach the protected site. A distance of few meters may be left between the embankment and the slope to collect the fallen blocks by simultaneously facilitating their maintenance (Hoek, 2007; Peckover and Kerr, 1977; Pierson et al., 2001).

In the literature, various options are considered for the design of reinforced soil embankments. The upstream facing is particularly investigated in order to better resist the impact or to facilitate the reparation. Some of the materials used in these facings are: tires, gabions, soil bags, steel mesh, mild steel, timber etc. (Aminata et al., 2008; Burroughs et al., 1993; Durville et al., 2010; Heymann et al., 2010; Peila et al., 2007; Yoshida, 1999).

The aspect ratio of the embankment plays an important role in its structural response during the impact. A slender embankment could be more prone to external instability such as leaning, bending or base sliding, while an embankment that has low slenderness would be more stable structurally. Traditionally, the reinforced soil embankments have a trapezoidal shape with a relatively low slenderness (Brunet et al., 2009; Maegawa et al., 2011; Peila et al., 2007; Tissières, 1999; Yoshida, 1999). By this approach, such protection systems require a fairly large area to be constructed due to their significant base width.

The reinforced soil embankments with vertical facings and slenderness higher than unity are not common in the literature and their impact resistance is still an open issue. Burroughs et al., (1993) tested an embankment with timber facing and internal geotextile reinforcement with impact energies up to 1.4 MJ, while Lambert et al., (2020) tested sandwich structures made of gabion cages with impact energies up to 2 MJ.

This article deals with slender reinforced soil embankments with vertical facings. The facings consist of welded steel mesh panels that are held in position by geosynthetic reinforcements. The benefit of this embankment with rectangular shape is the reduced footprint of the foundation compared to the usual ones with trapezoidal shape. This would reduce the required construction space in civil engineering projects. The increased flexibility of the embankment with vertical facings needs to be compensated by the role of the geosynthetic reinforcements installed inside. The key issue is to find the optimal reinforcement design, so that this slender embankment becomes an efficient rockfall protection barrier.

In the literature, the reinforced soil embankments are usually equipped with geosynthetic reinforcements placed periodically in continuous horizontal layers inside the embankment, which sometimes serve as wraparounds that maintain the steep angle of the faces (Brunet et al., 2009; Maegawa et al., 2011; Peila et al., 2007; Yoshida, 1999). Despite the research performed on reinforced soil embankments, the role of the reinforcements design in the impact resistance of the embankment is not yet fully studied. Blovsky (2002) tried to find the optimal design between different reduced scale soil embankments by using geotextile as reinforcement. He concluded that the reinforcement did not increase much the stiffness of the embankment, but it was particularly important in mobilizing a larger soil mass and thus altering the failure mechanisms. The reinforced embankments were more resistant under multiple impacts than the ones without reinforcement and the embankment failure occurred when the reinforcement failed or was no longer interacting with the soil due to large deformations.

Experiments on real scale with different types of reinforced soil embankments have shown that whatever the solution, there is a significant soil damage and plastification close to the impact position and a lower deformation far from it (Burroughs et al., 1993; Clerici et al., 2013; Hara et al., 2012; Peila et al., 2007). In fact, a design procedure is not yet generalized for the dimensioning of these types of protection systems, but there are empirical approaches based, for example, on the penetration of the impacting block and extrapolation from previous impact tests (Brunet et al., 2009; Korini et al., 2019; Lambert and Bourrier, 2013; Ronco et al., 2009; Tissières, 1999).

In this article, the effect of the reinforcements design to the impact behavior of rockfall protection soil embankments, is studied by performing impact tests under real conditions. Geogrids are selected to be used as internal reinforcements in this test campaign. Seeking the most efficient geogrid installation for the proposed embankment with vertical facings, two design options are chosen for being constructed and tested. The objectives of these tests are to point out which geogrid design results in lower embankment deformation after the impact and to compare the mobilization that the geogrids attain during the test. The two embankments differ from each other only in the internal geogrid reinforcements. Embankment 1 has vertical layers of geogrids, while Embankment 2 has horizontal ones. In both cases the aim is to distribute the effect of the impact in the longitudinal direction, which should mobilize more soil volume out of the impact zone and would contribute to reduce the embankment's overall damage. The vertical placement of the geogrids in Embankment 1 installed at a certain distance from the front facing, intents to act as a reinforcement sheet that inhibits the advancement of the sheared soil during the block's penetration. The horizontal orientation of the geogrids in Embankment 2 do not create a barrier for the sheared soil as in Embankment 1, but this could be compensated by a more efficient mobilization due to their closer distance to the impact position compared to the ones of Embankment 1.

In the following section, the designs of the studied reinforced soil embankments are presented in detail as well as the instrumentation used to monitor their behavior during the tests. Then the performed impact tests are described, followed by the main results of the monitoring devices. Lastly, the behavior of the two embankments is analyzed and compared for highlighting the specificities of each reinforcement design.

2 Design and construction of the reinforced soil embankments

2.1 Description of the two tested embankments

The two reinforced embankments tested have a rectangular cross section shape with a height equal to twice their width. With this shape, the embankments are more flexible, so the impact energy is eventually dissipated not only by the local plastification of the soil at the impact position, but also by the overall structural deformation enabled by the interaction of the reinforcements with the soil. Therefore, it is important to find the most effective reinforcement design, so that the impacting block may be stopped by causing minimal damage to the embankment.

The embankments are built using TerraTrel technology from Terre Armée. This technique uses welded steel mesh panels which are held vertically by geosynthetic strips (geostrips). The geostrip is a 0.05 m wide strip and has a tensile strength of 20 kN. The latter holds in position the steel mesh of the facings and has a similar installation for the two embankments (Figures 1 and 3c). Between the steel mesh panels, the embankments are backfilled with granular soil combined with layers of geogrids. The used geogrids consist of polyester yarns in a HDPE matrix and are created by welding perpendicularly 0.025 m wide strips to obtain apertures 0.05 m x 0.20 m. The result is a geogrid with a tensile capacity in the primary direction of 77 kN / m and 27.5 kN / m in the secondary direction (Korini et al., 2019). The primary direction of the geogrids is oriented in the longitudinal direction of the embankment, in order to mobilize laterally a greater amount of soil during the impact.

In reinforced soil structures the soil is recommended to have less than 12% of fines (EN 14475, 2007) so that the internal friction angle is high and the water drains quickly. Reinforced soil embankments with cohesive soils exhibit a highly plastic behavior when impacted and are not efficient in distributing the effect of the impact to a larger area due to their lower internal friction compared to granular soil (Peila et al., 2007). In this study, it is aimed to have an optimal distribution of the impact effect in the longitudinal direction of the embankment, so the cohesive behavior of the soil and consequently its fines content, is limited. The chosen soil was well graded with grain sizes between 0 – 40 mm and about 10% of fines.

The interaction between the soil and the geogrids depends on the friction and the interlocking between them. The friction component is a function of the soil friction angle and the geogrid's surface roughness, while the interlocking component depends on the soil grain sizes and the geogrid's apertures. For uniform soils, it is straightforward to define a relationship between the minimal aperture of the geogrid (A) and the grain size of the soil (D), while for well graded soils (as in this case), researchers (Athanasopoulos, 1993; Sarsby, 1985) have proposed the use of diameter D_{50} of the granulometry curve (50% of the soil mass would pass through a sieve with this aperture size). Using this parameter, different A/D_{50} ratios have been proposed for efficient interlocking between the soil and the geogrid. Sarsby, (1985) investigated the interaction of granular soil and uniaxial geogrid and found the optimal A/D_{50} to be 3.5, while Athanasopoulos, (1993) using geotextile as reinforcement proposed that A/D_{50} be equal to 1.6. Han et al. (2018) studied the soil-geogrid interlocking effect using uniform soils and biaxial / triaxial geogrids. They observed that the most effective ratio A/D_{50} was between 1.3 and 1.7 for biaxial geogrids. To avoid the development of a shear band, Springman et al., (1992) recommended limiting the geogrid

aperture to 5 times the diameter D_{50}. In our case the soil had a D_{50} of 15 mm, which means that the ratio A/D_{50} was 3.3 for the minimal aperture size of the geogrid. This value is quite close to the optimal one estimated by Sarsby, (1985) and fulfills the recommendation of Springman et al., (1992). The physical and mechanical characteristics of the soil measured in the laboratory and *in situ* are given in Table 1. It is to be noted that for the *in situ* density it is used a non-standard method, the "plastic sheet method". This method begins by digging a cavity in the compacted soil, while simultaneously collecting the removed material for determining its weight. Afterwards, a thin plastic sheet is placed over the cavity and it is filled with water. The volume of water that is necessary to fill the cavity is considered to be equal to the volume of the removed soil. The test is repeated three times for each embankment. The removed soil had an average weight of about 8 kg, while the volume of the water used to fill the cavity was about 3 liters. This simple method lacks accuracy due to the limited capacity of the plastic sheet to perfectly fit the cavity's volume. Consequently, the measured density with this method is thought to be overestimated.

Table 1. Summary of soil properties

Property	**Unit**	**Value**
Fines content	%	10.7
VBS	g / 100 g	0.234
In situ water content	%	3.7
In situ density	kg/ m^3	2 570
Standard Proctor optimal density (humid)	kg / m^3	2 400
Modified Proctor optimal density (humid)	kg/ m^3	2 510
Proctor optimal water content	%	3.7

In order to find the most efficient design, the two embankments are reinforced differently with regard to geogrids. In Embankment 1 the geogrids are installed vertically in two layers, while in Embankment 2, they are placed horizontally in several layers (Figure 1). The direction with the highest strength of these geogrids is installed in the longitudinal direction of the embankment in both cases. For a better comparison of efficiency, an approximately equal amount of geogrids is incorporated in each embankment.

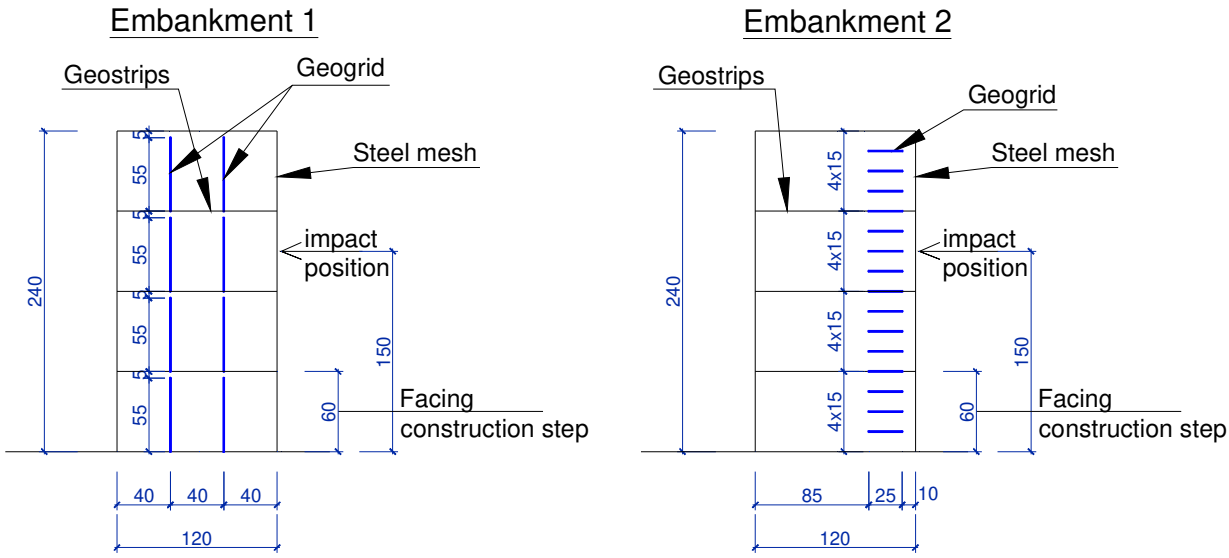

148

149 **Figure 1. Cross section design of the two embankments (units: cm)**

150 **2.2 Construction of the reinforced soil embankments**

151 The two reinforced soil embankments are built next to each other (Figure 2) according to their respective design (Figure 3a
152 and 3b). In between, they are separated by a double polystyrene layer to restrict the interaction between them during the
153 impacts. After each 0.60 m of backfill, another row of steel mesh panels is installed together with the continuous zig-zag
154 geostrip (Figure 3c). The latter are linked to the steel mesh facing through metallic connectors, which serve also as
155 attachments between the steel mesh panels of different levels.

156 There were notable difficulties during Embankment 1 construction in maintaining the vertical position of the geogrid
157 reinforcements. The chosen geogrid was quite flexible, so it bulged during the backfilling process and its final shape was not
158 flat and vertical. As a result, the pretension that was generated in the geogrid by the soil compaction was probably not
159 uniform.

160 On the contrary, the Embankment 2 construction was not difficult due to the horizontal orientation of the geogrid
161 reinforcements.

162

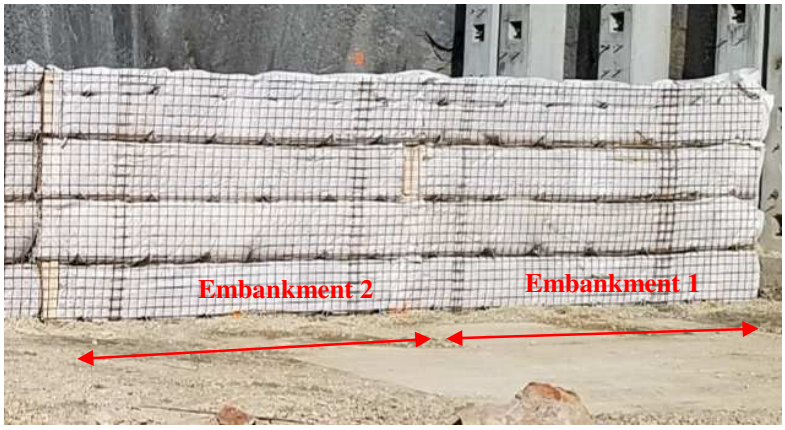

Figure 2. The two reinforced soil embankments before the impact tests

a)  b)  c) 

Figure 3. Construction of a) Embankment 1, b) Embankment 2 and c) facing retaining system for both embankments

3 Description of the impact tests and monitoring devices

3.1 Tests conditions

The horizontal impacts on the two reinforced soil embankments are performed on a test site using a large crane as a pendulum. The impactor is a reinforced concrete block with a mass of 1 639 kg, an outer dimension D of 0.95 m (hereinafter called “diameter”) and shape according to ETAG 27 (2013). The impactor was attached to a 60 m long steel cable and was pulled until it reached the launch position. This block reached the speed of 14.4 m/s just before the impacts, which means that the impacts had an energy of 0.170 MJ.

176 The impact axis was at the height of 1.50 m and in the middle of the embankment with regard to the longitudinal direction.
177 The impact height is chosen above the gravity center of embankment for testing the embankments' structural stability, which
178 could be vulnerable due to the slender cross section shape.

179 **3.2 Instrumentation and measurements**

180 The two reinforced soil embankments are monitored with several devices during and after the tests in order to determine the
181 behavior of the soil and the geogrids.
182 High-speed cameras (500 frames / second) are used to record the front and rear facings of the embankments during the
183 impact. This qualitative observation is complemented by the digitization of the shape of the embankments using a 3D laser
184 scan before and after the impact.
185 The pressure variation at the base of the embankments is measured by two pressure sensors placed at the foundation along
186 the impact axis of each embankment, one near the front face and the other near the back. The objective of the front sensor is
187 to observe if the impact generates an uplift of the base of the embankments, which would likely compromise the external
188 stability, while the rear sensor is used to measure the variation of the maximum stress on the foundation during the impact.
189 The deceleration of the impactor is recorded using an autonomous 3D accelerometer attached to the back face of the
190 impactor.
191 Five accelerometers are placed in each embankment at the impact height. Four of them are combined in couples oriented in
192 two perpendicular directions, aiming to measure the propagation of impact waves in the soil, while the role of the single
193 accelerometer close to the impact position is to record the peak acceleration and compare it to that of the others.
194 The variation of the strain in the geogrids during the impacts is measured using 28 strain gauges for each embankment.
195 Assuming a symmetric loading in the embankments, the strain gauges are placed in a T pattern around the impact position
196 for measuring the longitudinal and vertical variations of the strain. Two rows of strain gauges placed 0.45 m apart are used in
197 both directions to capture the maximum strain value. Embankment 1 has two vertical layers of geogrids, so the same strain
198 gauges distribution is installed in both of them (14 gauges / layer). For Embankment 2, which has horizontal layers of
199 geogrids, two parallel ribs of the same geogrid were equipped according to the same T pattern of Embankment 1. The
200 deformation sensitivity of strain gauges is in the range of micro-strain ($1\ \mu\varepsilon = 10^{-6}$ m/m $= 10^{-4}$ %).
201
202 In order to observe the detailed effects of the dynamic load, the acquisition frequency is set to 10 kHz and all the
203 instrumentations are synchronized before the test, except the two cameras and the 3D accelerometer inside the impactor.

4 Results

The instrumentation used for monitoring the response of the embankments was generally efficient and provided useful data. Only two strain gauges per embankment, out of 28 that were installed in the geogrids, failed during the impact. Some of the recorded data from the used devices are presented below.

4.1 Deformation and failure observations during the impact

The two embankments resisted successfully the impact. The rapid cameras revealed that the two reinforced soil embankments underwent three phases of deformation during the test (Figures 4 and 5). The first phase is characterized by the deformation of the embankment due to the block penetration. It is remarked that the back extrusion begins approximately 0.01 s after the start of the impact, when the block penetration is about 0.1 m. Afterwards, as the block continues to penetrate in the embankment it produces local shearing at the impact position and a wider and more gradual deformation at the rear face. The penetration of the block is also accompanied by a structural bending of the embankment (Figure 4 and 5) that is probably due to the presence of the steel mesh facing and geostrips, which maintain the structural integrity by distributing the effect of the impact. At the second phase, it is observed a backward leaning of the embankments, which was accompanied by the buckling of the welded steel mesh at the bottom of the rear face of the embankment. During this time, the block is still in contact with the embankment, but has already lost most of its initial speed. At the third phase, a partial return of the embankments was observed, while the impacting block moved slightly backwards without touching the embankment.

For the two embankments, the entire duration of the three phases was approximately one second. For Embankment 1, the duration of the penetration was about 0.150 s and the duration of the backward leaning phase was about 0.420 s. For Embankment 2, both phases were shorter compared to the ones of Embankment 1, with a duration was about 0.120 s for the penetration and about 0.390 s for the backward leaning.

Figure 4. Embankment 1 deformation at the end of: a) the first phase; b) the second phase; c) the third phase.

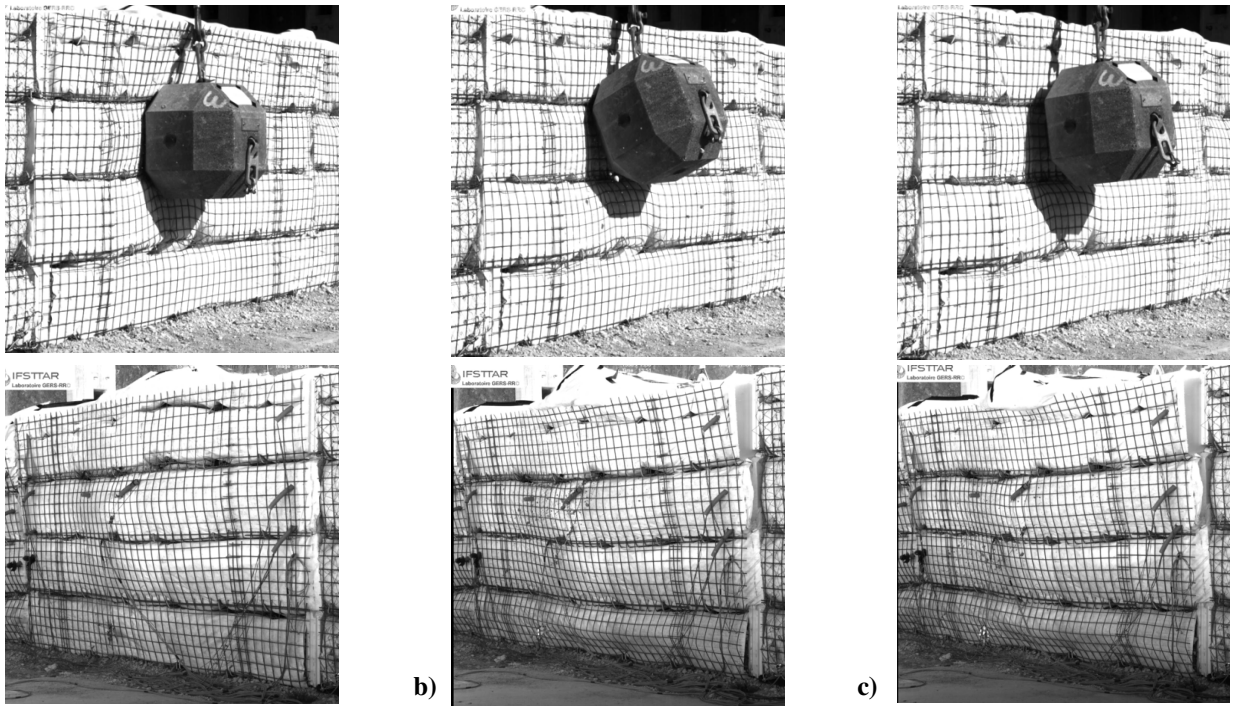

Figure 5. Embankment 2 deformation at the end of: a) the first phase; b) the second phase; c) the third phase.

The residual deformations of the embankments are digitized using a 3D scan device that is able to produce point clouds with a resolution in the order of a few millimeters. In order to find the displacement field (Figure 6), the data points are treated with a 3D image correlation technique. The images show that the two embankments have undergone significant displacements after the impact. The position of the penetration is clearly visible on the front faces. The displacement at the impact position for Embankment 1 (approximately 0.55 m) is greater than the one of Embankment 2 (approximately 0.40 m). The shape of the rear displacement field illustrates the backward leaning of the embankments through a gradual increase of

the displacements towards the top, as it was observed by the camera. This phenomenon is more important for Embankment 1 than for Embankment 2.

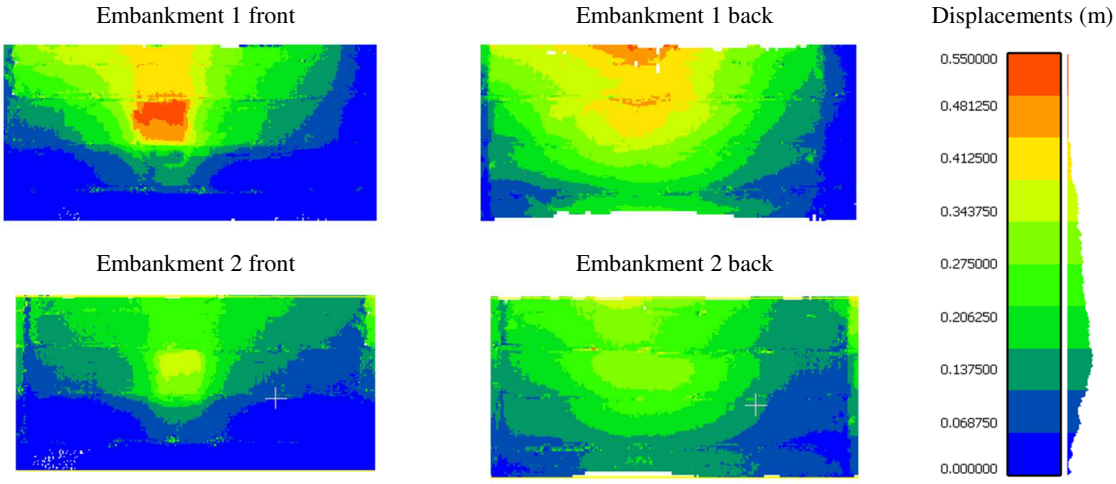

Figure 6. 3D displacements of the front and back faces for Embankment 1 and Embankment 2 derived from laser scan data

4.2 Impact loading

Considering the 3D accelerometer fixed on the impacting block, the direction that was perpendicular to the embankment's facing had the most relevant data to qualify the impact loading. A peak occurred around 0.02 s after the beginning of the impact (Figure 7) with a duration of around 0.08 s. The duration of the peak in this direction is similar for both embankments, but the peak value in the case of Embankment 2 is 40 % higher than that of Embankment 1. This indicates a stiffer response for Embankment 2 compared to Embankment 1.

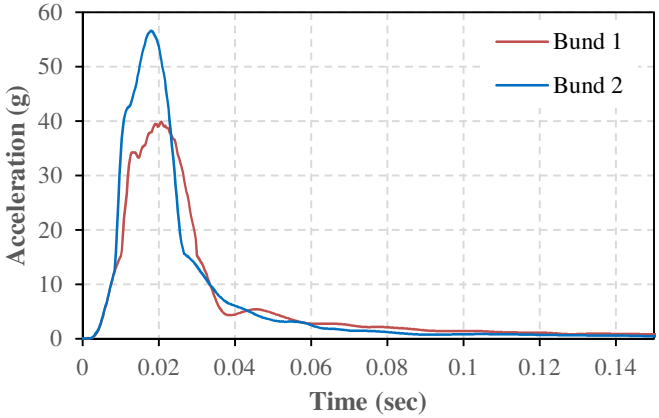

Figure 7. Impactor accelerometer data (Korini et al., 2019)

4.3 Acceleration inside the embankments

The uniaxial accelerometer that was placed 0.4 m far from the front face in the axis of the impact (Figure 8b: 'acc3') provided measurements that are close to each other for the two embankments (Figure 8a). A peak has occurred at 0.002 s for Embankment 2 and at 0.003 s for Embankment 1 after the beginning of the accelerometer loading. In both cases the duration of the peaks is around 0.01 s, whereas the peak value for the Embankment 1 is slightly higher (17 %) than that for the Embankment 2.

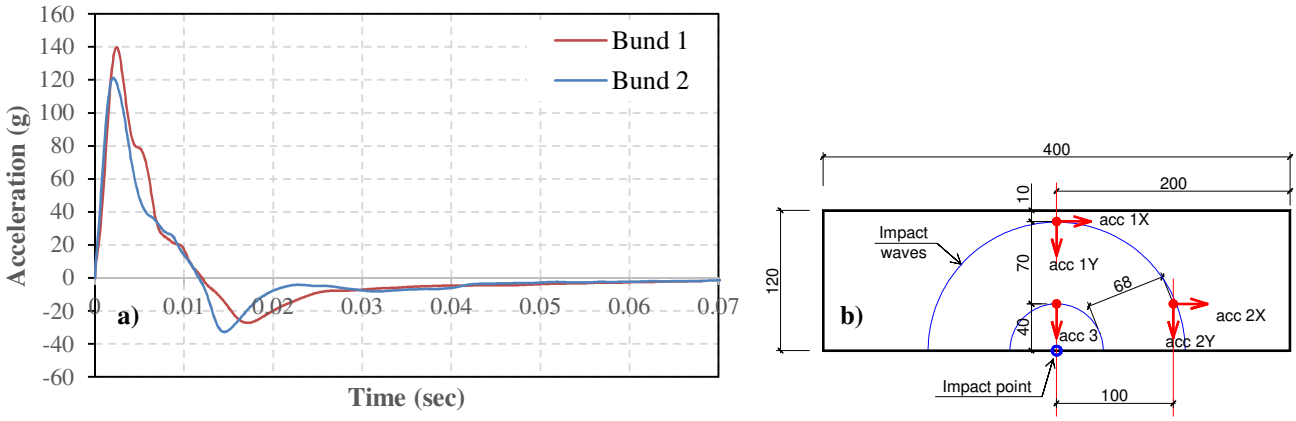

Figure 8. a) Acceleration of acc3 sensor for both embankments and b) position of the sensors in plan view

The speed of the impact wave can be calculated using the propagation distance between the accelerometers and the corresponding time interval. Assuming that this wave propagates in a spherical front which started at the axis of impact, the speed of the wave is calculated using the distance crossed by the wave from the accelerometer "acc3 "(Figure 8b) and the

time it took to reach "acc1 "and" acc2 " (Table 3). Based on the directions of the accelerometers, it can be assumed that "acc1X" and "acc2Y" respond to the shear wave, while "acc1Y" and "acc2X" respond to the pressure wave.

Table 3. Calculation of wave propagation speed from accelerometers for Embankment 1 and Embankment 2

Accelerometer	Speed (m/s)		Comments
	Embankment 1	Embankment 2	
acc1X	233	156	Shear wave
acc1Y	37	233	Pressure wave
acc2X	33	283	Pressure wave
acc2Y	234	227	Shear wave

The speeds of the impact waves on Embankment 1 are clearly divided into two groups. One group consists of the speeds measured by acc1X and acc2Y and the other consists of the speeds measured by acc1Y and acc2X. By comparing the two groups, it is observed that the pressure wave is much slower than the shear wave. This contradicts the common knowledge regarding the propagation of the waves in soils (Kramer, 1996; Uyanik, 2010). For Embankment 2, the pressure waves are faster than the shear ones, but the difference between them is not as important as in Embankment 1.

The speed of the impact waves in both embankments are in the same order of magnitude, except for the pressure waves at Embankment 1. The fact that the shear waves' speeds between the two embankments are comparable implies that the construction difficulties encountered at Embankment 1, did not have an important influence in parameters that could alter the wave speed, such as the soil density. Considering that the only difference between the two tested embankments is the internal reinforcement design, this could be the reason for the low values of the pressure waves' speeds at Embankment 1. Apparently, the geogrids installed vertically seem to attenuate the pressure wave that travels perpendicular to them, without visibly affecting the shear wave propagation. Remarkably, at Embankment 1 the placement of the acc2 accelerometers behind one layer of geogrids and of acc1 accelerometers behind two layers of geogrids did not have a notable influence on the speed of the waves.

The waves' propagation speeds in the case of Embankment 2 are less affected by the geogrids' installation (Table 3). Since the accelerometers are all installed at the impact height, it is probable that the impact waves were able to propagate without effort between the horizontally installed geogrids of Embankment 2, which did not act as barriers like in the case of Embankment 1. However, it is observed that the acc1 accelerometers recorded more attenuated wave speeds compared to the acc2 accelerometers, when comparing the waves of similar nature (Table 3). One possible explanation is that the horizontally placed geogrids at Embankment 2 acted as dampers in the vertical direction. Considering the fact that the impact wave travels in a three-dimensional front, the attenuation effect perpendicularly to the geogrids could affect the wave propagation speed. This attenuation is more visible for the acc1 accelerometers due to their greater distance from the geogrids.

295 **4.4 Pressure variation at the base of the embankments**

296 During the construction of the embankments, the pressure sensors were periodically checked in order to monitor the
297 variation of the vertical stress at the base of the embankment as a function of the construction height. For Embankment 1, at
298 the end of construction, the pressure at the base of the embankment was between 66 kPa (back sensor) and 79 kPa (front
299 sensor) and for Embankment 2, between 78 kPa (front sensor) and 84 kPa (back sensor). The theoretical average vertical
300 pressure at a given depth in granular soils is obtained by multiplying the unit weight of the soil by the depth. According to
301 the *in situ* density test, an approximate assessment of the natural density of the soil is 2 570 kg / m^3. This value is very close
302 to the maximum density obtained with the modified Proctor test (Table 1: 2 510 kg / m^3). Taking these values into account,
303 the stresses in all the pressure sensors at the end of construction exceed the theoretical value calculated with the density of
304 the modified Proctor test (59.1 kPa). Considering that the soil had about 10 % of fines (Table 1), this might have provided to
305 the soil a slightly cohesive behavior, which could partially trap the compaction pressures thus leading to higher than
306 expected base pressures.
307 During the impact, the pressure sensors are loaded between 0.001 s and 0.002 s after the loading of the accelerometer "acc3"
308 that is located close to the impact position (Figure 8b). For each sensor, a similar signal is observed (Figure 9). Considering
309 the rapid variation of the pressures, it is thought that the main cause of the initial oscillation is the propagation of the impact
310 waves in the embankments. For the two embankments, the duration of the peak is larger for the back sensor (~ 0.040 s) than
311 for the front one (~ 0.015 s/ 0.020 s). A possible explanation for this occurrence may be obtained by making an analogy of
312 the impact wave propagation with the seismic wave propagation in soils. In the latter, it is observed a decrease of the signal's
313 frequency (or increase of period) as the distance from the source increases (Kramer, 1996). Similarly, in our case the
314 duration of the peak (analogue to the period) is higher for the back sensors, which are located farther from the impact
315 position compared to the front ones.
316 The time lapse between the peaks of the front and back sensors for Embankment 1 is more important than for Embankment
317 2. In addition, the peak values are significantly different between the two embankments (Figure 9). For Embankment 1, the
318 front and back peak values are very close to each other, 307 kPa and 283 kPa, respectively. On the other hand, Embankment
319 2 has a peak value of 364 kPa for the front sensor and 567 kPa for the back one. At the end of the impact test, for
320 Embankment 1, the pressures are stabilized at around 12 kPa for the front sensor and at 131 kPa for the back sensor. The
321 residual pressures after the impact for Embankment 2 are 21 kPa for the front sensor and 81 kPa for the back sensor. The
322 front pressures after the impact are much lower than the initial values for both embankments. The final back pressures are
323 similar to the initial value for Embankment 2 and higher for Embankment 1. These differences between the sensors' data of
324 the two embankments indicate an influence of the different geogrid reinforcements design.

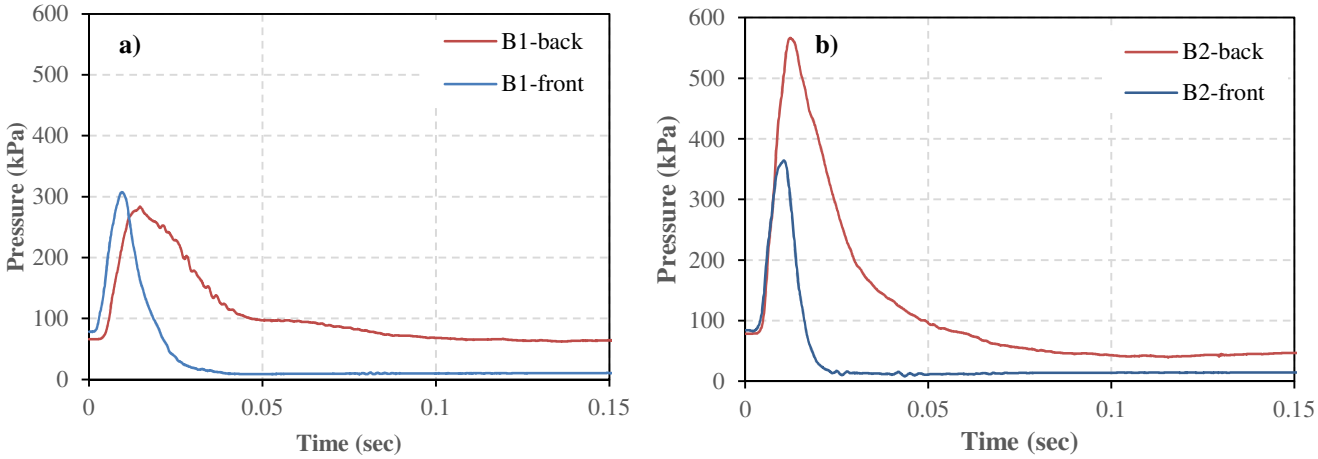

Figure 9. Variation of the base pressures during the impact: a) Embankment 1; b) Embankment 2.

4.5 Deformation of the geogrid reinforcements

The special glue used to fix the strain gauges to the geogrids has the deformation limit of 5.3 %, so the strain gauges measuring capability is restricted to this value. In addition, due to the adjustment of the acquisition system, the measurement range was further restricted to 4.4 %. This plateau is reached only by two strain gauges at Embankment 2, which were located the closest to the impact position (Figure 11). The gauge G15 measurements probably exceeded the deformation limit of 5.3 % because the measurement remained constant afterwards, which means that the strain gauge was detached from the geogrid. In this context, the attained peak strain of G15 is unknown. On the other hand, G16 returned to lower measurements after the plateau, so its peak strain remained within the deformation limit of the glue (5.3 %).

The strain gauges located outside the impact zone of both embankments underwent three successive deformation stages (Figures 10 and 11). During the first stage of approximately 0.01 s, a rapid relaxation of the strains was observed at a higher rate the closer the gauges were to the impact position. In the second stage, the gauges were mobilized in tension with a peak that was again higher for the strain gauges closer to the impact position. In the last stage, a progressive strain relaxation was noted, and the measurements were stabilized at low residual values. For the strain gauges in the impact zones of both embankments (G4, G15 and G16), the first stage of relaxation did not occur, but instead they experienced a very rapid tensile loading.

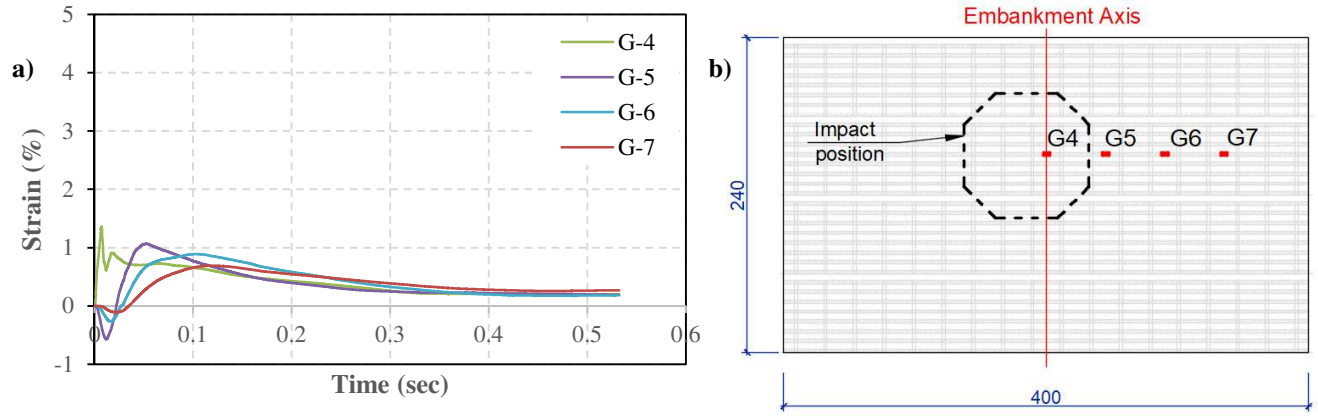

Figure 10. a) Measurements of the front strain gauges of Embankment 1 and b) their position

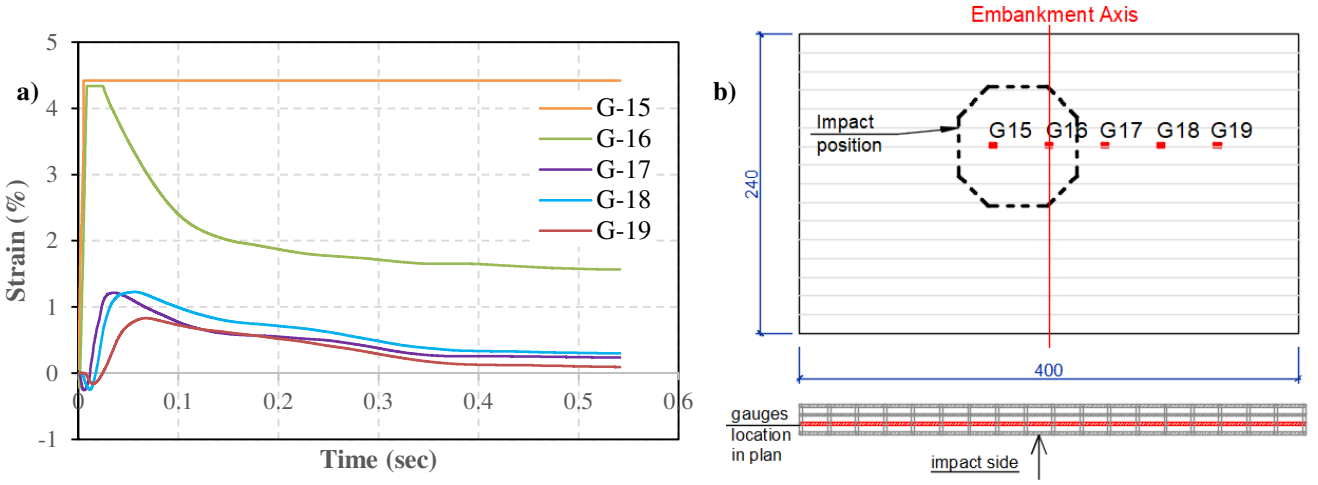

Figure 11. Embankment 2: a) Measurements of the front strain gauges of Embankment 2 and b) their position

For the two embankments, the maximal strain values are close between the front measurement zone and the back measurement zone (Figure 12). The values are higher for the strain gauges installed close to the impact height (§2.1: 1.50 m). The shape of the maximal strains curve along the embankments is different between the two embankments. For Embankment 2, this shape indicates a much-localized significant deformation in the impact zone. For Embankment 1, the maximal strains curves have lower values than those of Embankment 2 and exhibit a more gradual variation without significant localization at the impact position (Figure 12a). The maximum recorded strains are 1.9 % for Embankment 1 and 4.4 % for Embankment 2 (Figure 12).

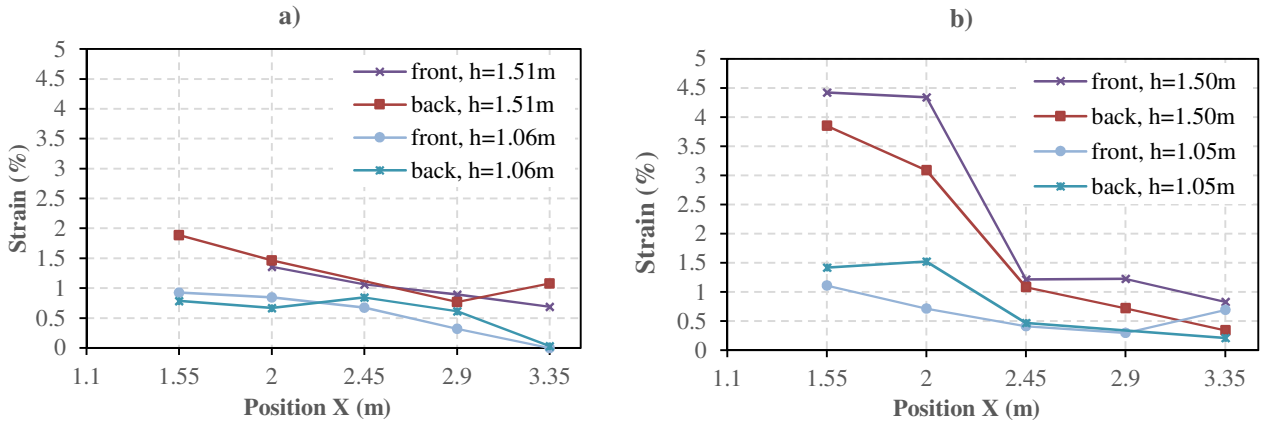

Figure 12. Variation of maximal strain measured along the longitudinal direction for: a) Embankment 1; b) Embankment 2

5. Discussion on the behavior of embankments against impact

5.1 Impact resistance and deformation patterns

During the reduced-scale tests the impacting block was successfully stopped by each of the two 2.40 m high embankments, which indicates that the impact resistance of these two embankments is greater than 0.17 MJ.

The 3D displacements during the impacts (Figure 6) being considered, no displacement of the embankments is observed at the base. This shows that the embankments did not experience sliding at the base. The displacements after the tests are more concentrated in the upper part of the embankments. According to the recordings of the cameras, they may be described as a combination of local shear deformation due to the penetration of the block and a backwards leaning of the embankment.

The front deformations of the embankments are higher at the impact position and gradually decline in the surrounding area (Figure 6). By observing the back extrusion of the impacted embankments, one can identify that it presents a smooth variation of displacements in every direction and not a differential slippage of the reinforced soil layers of the impact zone, as observed in Peila et al., (2007). In the latter, the continuous horizontal geogrids divided the soil of the embankment in layers and apparently allowed the creation of sliding planes between these layers during the impact. In the embankments of the current study, the geogrids are installed differently (Figure 1), so the creation of the horizontal sliding mechanism is not favored (Figures 4 and 5). Consequently, the effect of the impact is more distributed and a larger embankment's volume contributes to stop the impacting block.

373 **5.2 The three phases of the embankments' behavior against the impact**

374 The behavior of the tested embankments against the impact can be discretized in three main phases. The following
375 description presents commons points and complements that of Lambert and Bourrier, (2013).
376
377 Phase 1 – The penetration of the block
378 This phase initiated at the moment when the impacting block touched the embankment's facing and lasted for a few tenths of
379 a second (§4.1). During the first hundredths of a second of this phase, there are observed oscillations on multiple sensors
380 inside the embankment probably due to the propagation of the impact waves. According to the accelerometers in the
381 embankments (§4.3), the soil close to the impact position experienced a peak acceleration higher than 100 g (Figure 8). The
382 front and back pressure sensors reacted after the accelerometers with single transient peaks (Figure 9). These peaks do not
383 correspond to the embankment's backwards leaning, which happens at a later moment according to the rapid cameras. The
384 impact waves' effect is also observed at the measurements of the strain gauges glued on the geogrids outside the impact
385 zone, which indicated a peak strain relaxation in the first moments of the impact (Figures 10 and 11). The moment of this
386 strain relaxation corresponds approximately to the moment of the peak measurements of the pressure sensors, which is
387 another indication that a common cause is behind these occurrences. For the strain gauges in the impact zone, the strain
388 relaxation is not observed (G4, G15 and G16: Figures 10 and 11). One possibility is that the pressure applied in this area by
389 the impacting block while penetrating the embankment, surpasses the effect of the impact wave thus making the latter
390 unperceptive by the strain gauges.
391 As the block continued to penetrate the embankment, it caused further shearing at the impact position, but also general
392 structural bending. The strain gauges were more sensitive to this deformation of the embankment compared to the pressure
393 sensors and accelerometers. Directly after the strain relaxation that is observed during the propagation of the impact wave
394 along the geogrids, all the strain gauges experienced peak tensile deformations, which had higher values the closer the
395 gauges were to the impact position (Figures 10 and 11). These peaks are a consequence of the block penetration and
396 structural deformation of the embankment, since they occur after the impact waves' propagation. However, it is difficult to
397 distinguish the exact moment, when the effect of the impact wave becomes negligible at the loading part of the tensile peaks.
398 On the other hand, the unloading part of the curves is much slower than the loading one and seems to be unaffected by the
399 earlier dynamic phenomena. This is confirmed by the other measurements, which show that the signals of the accelerometers
400 and pressure sensors start to get stabilized after 0.05 s (Figure 7, 8 and 9).
401
402 Phase 2 - The backwards leaning of the embankment
403 During this phase, the embankments continue to deform by leaning backwards for about 0.4 s (§4.1). This deformation is not
404 due to influence of the impacting block because, at the beginning of this phase (0.12 – 0.15 s), it had already lost most of its
405 speed according to the rapid camera and the block's accelerometer data (Figure 7). However, during the first phase the

406 impacting block transmitted to the embankments the largest part of its kinetic energy, which in turn started to lean backwards
407 due to inertia.
408 The rapid cameras revealed that the largest part of the backward leaning of the embankments is due to the local failure of the
409 facing panels at the back. During the last moments of the block penetration phase, the bottom steel mesh panels at the back
410 of the embankments buckle, which weakens the facing stability and leads to a vertical settlement at the respective position
411 (Figure 4 and 5). The localized vertical settlement at the position of the failed back panels is followed by the backwards
412 leaning of the part of the embankment above these panels. The buckling of the steel mesh panels seems to be favored by two
413 main conditions. Firstly, the panels' movement is blocked in the upper and lower levels by the geostrips (Figure 3c), which
414 create the setting of an element with pinned support boundaries. Secondly, the back extrusion displaces towards the back the
415 gravity center of the embankment, which increases the vertical pressure at the back facing of the embankment thus leading to
416 the buckling of the bottom back steel mesh panel (Figures 4 and 5).
417 During this phase (approximately between 0.1 – 0.5 s), the measurements of the strain gauges show a slight decline (Figures
418 10 and 11). This means that unless they slide towards the soil, the geogrids slightly oppose the deformation that the
419 embankment experienced during the block penetration phase. It should be noted that this contribution of the geogrids in the
420 reduction of the embankments' deformation is restricted in the longitudinal direction of the embankment, since the geogrid
421 strips are discontinuous and do not have the necessary embedment length in the vertical direction.
422 It can be pointed out that the deformation experienced during this phase was probably favored by the relatively large size of
423 the impacting block compared to the size of the embankments in these tests. Their relatively low inertia made the
424 embankments more flexible and vulnerable with regard to structural stability.
425
426 Phase 3 – The partial return of the embankment
427 This phase takes place after about 0.5 s from the beginning of the impact and it is characterized by a partial return of the
428 embankments towards the initial position, which lasts for another 0.5 s. During this phase, the embankments incline slightly
429 forward while maintaining the shape that they obtained at the end of the previous phase. This partial return resembles to a
430 system that is able to store a certain amount of elastic energy during the loading phase, in order to release it later. Since the
431 granular soil by itself cannot store elastic energy, this behavior of the embankments is attributed to the reinforcements.
432 During this phase, the geogrids' strain measurements do not show any variation (time > 0.5 s: Figures 10 and 11), so they do
433 not contribute in the partial return of the embankments. This is coherent, because they are discontinuous in the vertical
434 direction that is affected by the partial return (Figure 1). On the other hand, the steel mesh panels of the facing present a
435 continuity in the vertical direction through the steel connectors that also link them to the geostrips (Figure 3). This system
436 that preserves the structural integrity of the embankment is probably the one that stores a part of the impact energy and
437 releases it later through a reduction of the backwards leaning of the embankments.
438

5.3 The influence of the geogrids' design to the embankments' behavior

The two embankments differ from each other only by the geogrid design, so the differences in their behavior are a consequence of the design variation. Even though the two embankments underwent the same phases during the impact, their level of deformation was different and in addition, notable differences are observed on the sensors' measurements of the two embankments.

The level of the deceleration of the impacting block shows how quickly its speed changes. It is thus proportional to the stiffness of the embankments. During the impact of Embankment 2, the deceleration of the block is higher than that of Embankment 1 (Figure 7). Physically, this means that Embankment 1 is more flexible and undergoes more deformation than Embankment 2 during the impact. This observation is emphasized by the lower level of penetration and rear displacement for Embankment 2 (Figure 6).

During the block penetration phase, the different effects of the impact wave on the analogue sensors installed at the two embankments (accelerometers and pressure sensors) reflects the fact that the wave propagation is modified by the presence of the geogrids. For the accelerometers in Embankment 1, it is noticed that the geogrids reduce significantly the speed of the pressure wave, while having negligible effect on the shear wave speed (Table 3). During the impact wave propagation, the pressure sensors of both embankments recorded peaks that are much higher than the initial construction pressures (Figure 9). The pressure sensors in Embankment 1 recorded similar peaks, while the sensors in Embankment 2 indicated a higher value at the back than at the front. It is remarkable that the front pressure sensors of both embankments recorded comparable values, but the back ones had an important difference. A possible reason would be that in the case of Embankment 1, the impact wave needs to cross two layers of geogrids in order to reach the back sensor, while in the case of Embankment 2, it is probably easier for the wave to pass through the horizontally installed geogrids. In this context, the stresses generated by the impact waves in the soil seem to be attenuated when they pass through geogrids that are installed perpendicularly to their propagation.

The geogrids of Embankment 2 had a limited role in the modification of the impact wave propagation. The data from the accelerometers did not reveal indications that could be attributed to the presence of the geogrid. Similarly, the signals of the pressure sensors of this embankment seem to be unaffected by the geogrids. This is proved by the similar peaks of the front pressure sensors of the two embankments. It is probable that the lower width of the geogrids of Embankment 2 (0.25 m) compared to the ones of Embankment 1 (0.55 m), may be responsible for their limited role in the impact wave propagation. Further tests are required to prove this hypothesis.

During the phase of the block penetration, for the same impact conditions, a significantly greater deformation of the geogrids is observed for Embankment 2 in the impact area. In Embankment 1, the maximum deformation of the geogrids in the impact axis is lower, which leads to a more homogeneous deformation along the geogrids (Figure 12). Several reasons could have caused this difference in geogrid mobilization. Firstly, the installation distance of the geogrids from the front facing is lower in Embankment 2 compared to Embankment 1 (Figure 1), so the effect of the block penetration is higher on the

geogrids of Embankment 2 that are located in the impact area. Secondly, the horizontal orientation of the geogrids in Embankment 2 was more favorable during the installation, producing a flat sheet that could be mobilized faster in tension during the impact. In Embankment 1, the initial irregular shape of the geogrids due to installation difficulties may have caused them to have lower and non-uniform pretensioning, which might have contributed to their lower mobilization. Lastly, the two vertical layers of geogrids in Embankment 1 divide the embankment into three vertical parts, which could lead to a reduction of interaction between the soil and the geogrids, due to the soil inertial movement during the penetration of the impacting block.

The vertical orientation of the geogrids in Embankment 1 resulted in a more distributed mobilization compared to the geogrids of Embankment 2. Probably, in Embankment 1 the geogrid ribs of the secondary direction played a role in distributing the impact load in all the ribs of the primary (longitudinal) direction. In Embankment 2, the horizontal placement of the geogrids did not allow this distribution to happen because the ribs of the secondary direction were initially compressed by the block penetration. This explains the difference of the mobilization of the instrumented front and back ribs of the same geogrids at Embankment 2 (Figure 12).

The distance from the impact is of great importance, when it comes to geogrid mobilization. The strain gauges that have the highest loading are those of Embankment 2, located at a distance of less than a block's radius from the intersection of the impact axis to the front facing (Figures 12, 13). Out of this zone, the loading of the geogrids drops quickly with respect to the peak strains and strain rates. Apparently, the impacting block creates a plastified zone at the impact position, in which both soil and reinforcements are subjected to large stresses and strains. This zone is part of the Impact Disturbed Zone (IDZ) that is a volume in the embankment, which is exposed to the direct influence of the impact load and consequently, it experiences larger deformations compared to the rest of the structure (Lambert and Kister, 2017). The IDZ shape is generally approximated to a truncated cone that begins with the imprint of the block at the front face and ends at the limits of the extrusion at the back face (Blovsky, 2002; Peila et al., 2002). The IDZ of Embankment 1 is larger compared to the one of Embankment 2 (Figures 4a and 5a), due to the higher block penetration in the former (Figure 6). The geogrids of Embankment 2 were able to reduce the block penetration and the size of the IDZ better than the geogrids of Embankment 1, due to the lower distance from the impact and their flat initial position, which allowed for a faster mobilization.

The stiffness and strength of geogrids depend on loading rate (Hirakawa et al., 2003). A higher loading rate usually leads to a stiffer and stronger geogrid. For this reason, the maximal strain rate is determined for each gauge as the average slope of the part of the strain curve that is located just before the peak strain. The variation of the maximal strain rate with respect to the gauges distance to the impact position (intersection of the impact axis with the front facing) is plotted (Figure 13). It is noticed that there is a correlation between the maximal strain rate of the strain gauges and their respective distance from the impact position. In both cases the maximal strain rate drops to less than 200%/sec for distances larger than 0.5 m. Remarkably, this value corresponds approximately to the radius of the impacting block (0.475 m). Unfortunately, only one strain gauge of Embankment 1 is located less than 0.5 m from the impact position (Figure 13), so the effect of the geogrids orientation at high loading rates cannot be adequately compared between the two embankments. For the strain gauges

located at distances greater than 0.5 m from the impact position, the loading rates of the geogrids are similar between the two embankments.

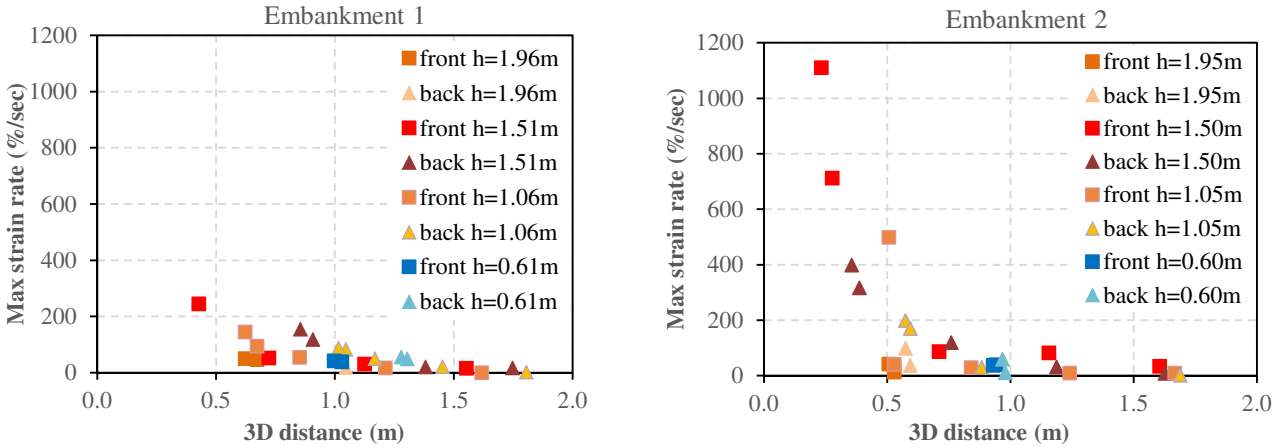

Figure 13. Relation of maximal strain rate with the distance to the impact position for the two embankments

As the failure criterion of geogrids depends on the loading rate, the most unfavorable moment for a geogrid during an impact is when it experiences the maximal strain at the maximal strain rate. For each strain gauge, the couple (maximal strain, maximal strain rate) was determined and plotted in Figure 14. The data can be grouped into one zone created by two second order polynomial curves, leaving out only one strain gauge. This gauge (G5) belongs to Embankment 2 and begins to mobilize about 0.002 seconds later than the one next to it (G6), which has almost the same distance to the impact position. One possibility is that this delayed and then rapid loading of strain gauge G5 could be due to different local interlocking of the soil aggregates to the geogrid. A concentration of coarse aggregate close to the strain gauge G5, could allow it to slide at the first moment (the initial delay) and then to have a rapid loading as the geogrid nearby is mobilized. However, this hypothesis could not be verified during the deconstruction because the impact altered significantly the initial conditions in this area.

No failure is observed on the installed geogrids of both embankments after the tests, so the ultimate resistance of the geogrids under dynamic loading conditions is not reached. In order to obtain the dynamic failure criteria for the geogrids, multiple rapid loading tests need to be performed on them so that the couple maximal strain – maximal strain rate is obtained for different loading conditions. The presence of this curve on Figure 14 would allow to judge how far the geogrids are from failure.

In the case of reinforced soil, the mobilization of the geogrids in dynamic loading depends on the soil properties. A well graded soil with a granulometry that allows for an efficient interlocking and friction with the geogrids, is able to transmit quickly the dynamic load thus causing high strain and strain rates on the geogrid. In this context, the polynomial curves that

encompass the maximal loading conditions of Figure 14 would be steeper if the soil – geogrid interaction is more efficient and vice versa.

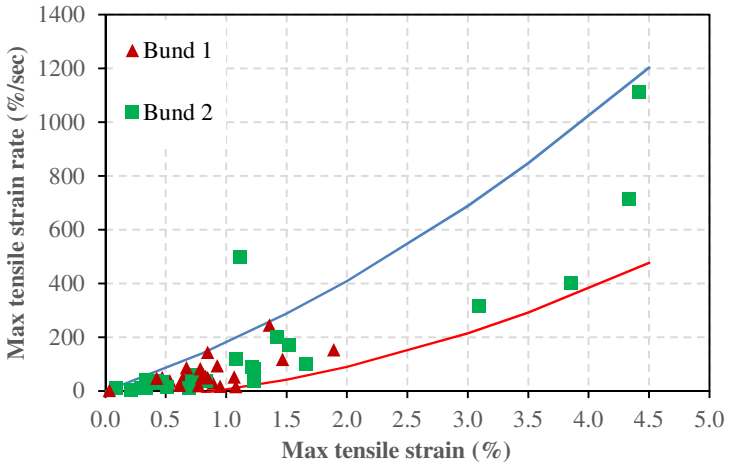

Figure 14. Strain rate – max strain for all the gauges of the two embankments

The speed of the impact wave may be also evaluated using the strain gauges measurements. Similarly, as with the accelerometers and the pressure sensors, the arrival time of the signal to each strain gauge was identified. By plotting this time versus the 3D distance to the impact position, a linear relationship is obtained (Figure 15). The inverse of the slope of this line is equal to the speed of the propagation of the impact wave. For Embankment 1, it is 182 m/s and for Embankment 2 it is 208 m/s. These values are close to the ones obtained from the accelerometers (Table 3).

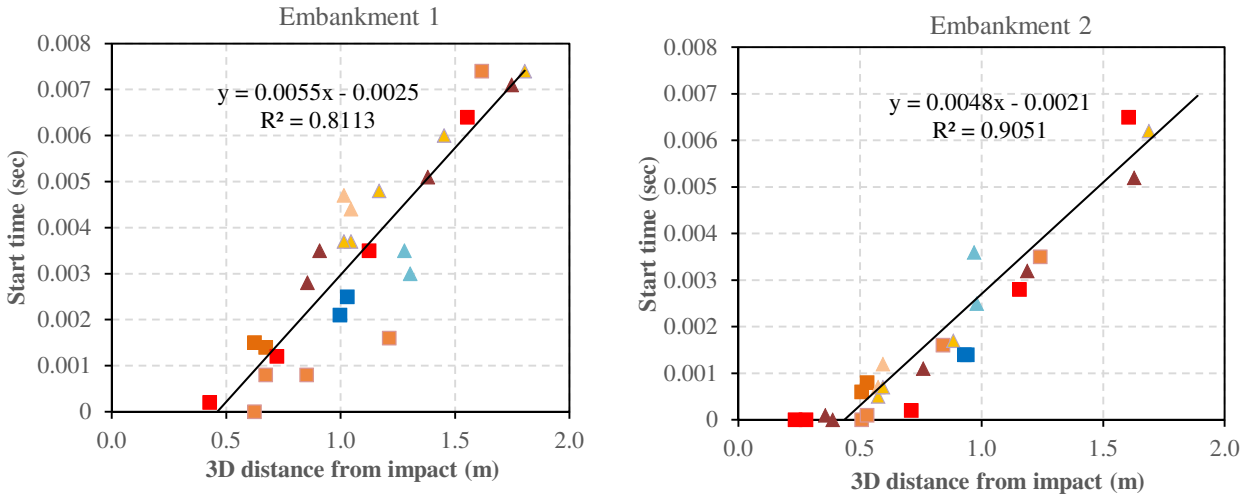

Figure 15. Strain gauges start of mobilization in function of their distance from the impact for the two embankments

543 The fact that the geogrids were able to experience the influence of the impact waves' propagation at the same time as other
544 sensors, means that the soil – geogrid interaction is satisfactory at the beginning of the impact. Moreover, this also signifies
545 that the stiffness of the used geogrid is adequate and facilitates this interaction.

546 **6. Conclusions**

547 The impacts induced dynamic effects on the tested embankments, which were recorded by different sensors installed inside
548 the embankments. During the first moments of the block penetration, there occurred a propagation of impact waves in the
549 embankments. Although this phenomenon did not have a marked influence in the impact resistance of the embankments, it
550 revealed that it may cause important pressures at the base that exceed several times the gravity stresses. Theoretically, the
551 impact waves travel in all directions in the embankment and if adequate reinforcements are missing, the embankment would
552 likely be prone to additional damage because of these waves. The measurements of the accelerometers and pressure sensors
553 showed that the geogrid reduces the pressure wave's propagation speed and the stresses induced by this wave in the soil if
554 the geogrid is installed perpendicularly to the wave's propagation and if it has the necessary width. On the other hand, the
555 impact wave had limited effect on the geogrids loading, which was visible on the initial relaxation part of the strain gauges'
556 data. Further tests for different types of soil and reinforcements are necessary to investigate the role of the geogrids in the
557 partial attenuation of the impact waves.
558 The horizontal installation of the geogrids close to the front facing proved to be more efficient than the vertical installation in
559 two layers inside the embankment. The former design resulted in a lower embankment's deformation and a better geogrid
560 mobilization in the vicinity of the impact. The distance of the geogrid from the impact position seems to affect the most its
561 mobilization. It is observed that high geogrid strains are concentrated at a distance of one block radius from the impact
562 position. This may serve as a design recommendation in the cases when high speed impacts are foreseen, and the geogrid
563 needs to be protected.
564 The strain rate is an important parameter for the characterization of the dynamic loading of the geogrids. By combining it
565 with the corresponding maximal strain, it is obtained the peak dynamic loading condition for the geogrid. It would be
566 beneficial to perform more experiments in order to build the dynamic failure curve using these two parameters. This curve
567 could be used for design purposes to choose the appropriate geogrid that will resist a specific dynamic loading.
568 The structural stability of the embankments was more critical than the local shearing due to the block penetration.
569 Apparently, the inertia of the tested embankments was not sufficient to prevent the backward leaning that they experienced.
570 It seems that the embankments had a relatively small size and a relatively high slenderness for resisting the chosen impacting
571 block. This issue could be addressed by increasing the embankment's length or reducing its slenderness ratio.

Acknowledgements

This research is part of a PhD study funded by "Terre Armée" company, which contributed with their expertise, technology and materials. The financial support of ANRT (French National Association for Research and Technology) provided as a grant for the PhD student is also acknowledged. The authors wish to thank the staff of University Gustave Eiffel of Bron (France) that contributed to this study, especially Patrick Joffrin and Christophe Pruvost for the high professionalism regarding the tests' instrumentation.

References

Aminata, D., Yashima, A., Sawada, K., Sung, E., Sugimori, K., Inoue, S., 2008. New protection wall against rockfall using a ductile cast iron panel. Journal of Natural Disaster Science 30, 25–33.

Athanasopoulos, G.A., 1993. Effect of particle size on the mechanical behaviour of sand-geotextile composites. Geotextiles and Geomembranes 12, 255–273. https://doi.org/10.1016/0266-1144(93)90029-N

Blovsky, S., 2002. Bewehrungsmöglichkeiten mit Geokunststoffen. PhD thesis (in German).

Brunet, G., Giacchetti, G., Bertolo, P., Peila, D., 2009. Protection from High Energy Rockfall Impacts using Terramesh Embankments: Design and Experiences, in: 60th Highway Geology Symposium, New York State Department of Transportation, New York State Museum.

Burroughs, D., Henson, H.H., Jiang, S.S., 1993. Full scale geotextile rock barrier wall testing, analysis and prediction, in: Proceedings of Geosynthetics. pp. 959–970.

Chen, Y.C., Li, J.K., Ran, L.G., 2013. A Review of Rockfall Control Measures along Highway. Applied Mechanics and Materials 353–356, 2385–2391. https://doi.org/10.4028/www.scientific.net/AMM.353-356.2385

Clerici, A., Giuriani, E., Cambiaghi, D., Isceri, A., Vassena, G., Marchina, E., Cominoli, L., 2013. Rockfall full scale field tests, in: Landslide Science and Practice. Springer, pp. 461–467.

Descoudres, F., 1997. Aspects géomécaniques des instabilités de falaises rocheuses et des chutes de blocs. Publications De La Société Suisse De Mécanique Des Sols et Des Roches 3–11.

Durville, J.L., Guillemin, P., Berthet-Rambaud, P., Subrin, D., 2010. Etat de l'art sur le dimensionnement des dispositifs de protection contre les chutes de blocs. Collection Études et recherches des LCPC—série Géotechnique et risques naturels, Paris (84 pp.).

EN 14475, N., 2007. Execution of special geotechnical works. Reinforced fill.

Hara, T., Tsuji, S., Yoshida, M., Ito, S., Sawada, K., 2012. Experimental development of new type reinforced soil wall. Int. J. of GEOMATE 2, 213–218.

Heymann, A., Lambert, S., Gotteland, P., Collombet, M., Douaillat, M., 2010. Expérimentations grandeur réelle sur merlons de protection contre les chutes de blocs rocheux, in: Journées Nationales de Géotechnique et de Géologie de l'Ingénieur JNGG 2010. p. p-665.

Hirakawa, D., Kongkitkul, W., Tatsuoka, F., Uchimura, T., 2003. Time-dependent stress–strain behaviour due to viscous properties of geogrid reinforcement. Geosynthetics International 10, 176–199.

Hoek, E., 2007. Practical rock engineering. 2007.

Korini, O., Bost, M., Rajot, J.P., Braouli, Y.B., Freitag, 2019. Experimental study of reinforced soil bunds subjected to horizontal impact. Presented at the International Congress on Rock Mechanics and Rock Engineering, Iguassu, Brazil.

Kramer, S.L., 1996. Geotechnical earthquake engineering. Pearson Education India.

Lambert, S., Bourrier, F., 2013. Design of rockfall protection embankments: a review. Engineering geology 154, 77–88.

Lambert, S., Bourrier, F., Gotteland, P., Nicot, F., 2020. An experimental investigation of the response of slender protective structures to rockfall impacts. Canadian Geotechnical Journal 1–17.

Lambert, S., Kister, B., 2018. Efficiency assessment of existing rockfall protection embankments based on an impact strength criterion. Engineering geology 243, 1–9.
Lambert, S., Kister, B., 2017. Analysis of Existing Rockfall Embankments of Switzerland (AERES) Part A: State of Knowledge. Analysis 2, 55.
Maegawa, K., Tajima, T., Yokota, T., Tohda, M., 2011. Experiments on rockfall protection embankments with geogrids and cushions. Int. J. Geomate 1, 19–24.
Peckover, F.L., Kerr, J.W.G., 1977. Treatment and maintenance of rock slopes on transportation routes. Canadian Geotechnical Journal 14, 487–507.
Peila, D., Castiglia, C., Oggeri, C., Guasti, G., Recalcati, P., Rimoldi, P., 2002. Testing and modelling geogrid reinforced soil embankments subject to high energy rock impacts, in: 7th International Conference on Geosynthetics.
Peila, D., Oggeri, C., Castiglia, C., 2007. Ground reinforced embankments for rockfall protection: design and evaluation of full scale tests. Landslides 4, 255–265.
Ronco, C., Oggeri, C., Peila, D., 2009. Design of reinforced ground embankments used for rockfall protection. Natural Hazards and Earth System Sciences 9, 1189–1199.
Sarsby, R.W., 1985. The influence of aperture size/particle size on the efficiency of grid reinforcement, in: Proc., 2nd Canadian Symp. on Geotextiles and Geomembranes. pp. 7–12.
Springman, S.M., Bolton, M.D., Sharma, J., Balachandran, S., 1992. Modelling and instrumentation of a geotextile in the geotechnical centrifuge, in: Proc. Int. Symp. on Earth Reinforcement Practice, Kyushu. p. 172.
Tissières, P., 1999. Ditches and reinforced ditches against falling rocks, in: Joint Japan-Swiss Scientific Seminar on Impact Load by Rock Falls and Design of Protection Structures, Kanazawa, Japan. pp. 4–7.
Uyanik, O., 2010. Compressional and shear-wave velocity measurements in unconsolidated top-soil and comparison of the results. International Journal of Physical Sciences 5, 1034–1039.
Yoshida, H., 1999. Recent experimental studies on rockfall control in Japan, in: Joint Japan-Swiss Scientific Seminar on Impact Load by Rock Falls and Design of Protection Structures, Kanazawa, Japan.